Article

Cell

Unfolding of a Temperature-Sensitive Domain Controls Voltage-Gated Channel Activation

Graphical Abstract

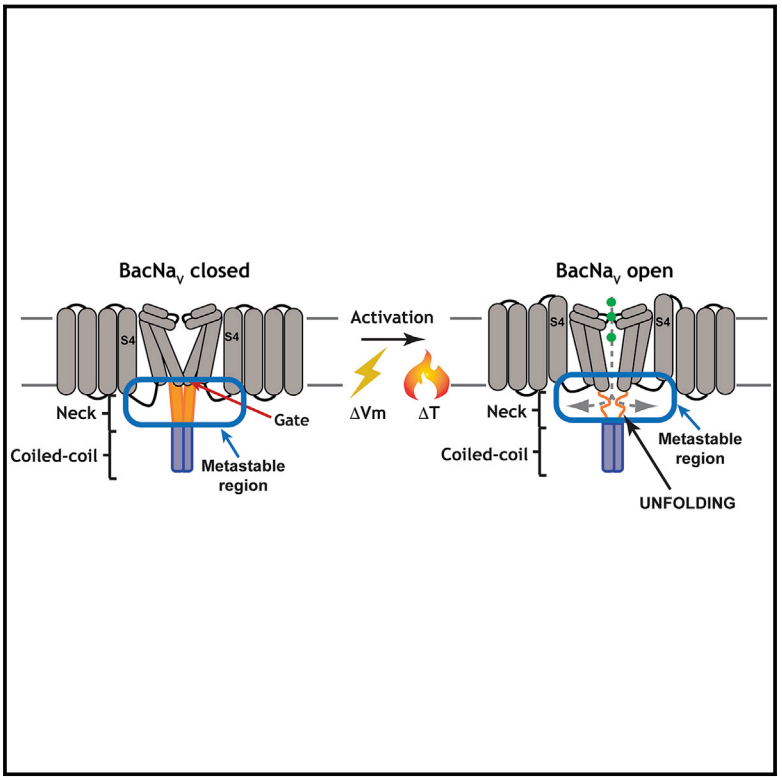

Authors

Cristina Arrigoni, Ahmed Rohaim, David Shaya, ..., Smriti Mishra, Hassane S. Mchaourab, Daniel L. Minor, Jr.

Correspondence

daniel.minor@ucsf.edu

In Brief

A cytoplasmic domain of bacterial sodium channels controls channel gating directly through a temperature-dependent reversible structural transition in a metastable region proximal to the pore.

Highlights

- The BacNa$_V$ cytoplasmic domain has profound effects on voltage-dependent gating
- An unfolding transition in the cytoplasmic domain metastable hydrophilic core tunes BacNa$_V$ gating
- BacNa$_V$ cytoplasmic domain unfolding is localized and temperature dependent
- A discrete domain can encode the temperature-dependent response of a channel

Accession Numbers

5HJ8
5HK6
5HKD
5HK7
5HKT
5HKU

Arrigoni et al., 2016, Cell *164*, 922–936
February 25, 2016
http://dx.doi.org/10.1016/j.cell.2016.02.001

CellPress

Cell

Article

Unfolding of a Temperature-Sensitive Domain Controls Voltage-Gated Channel Activation

Cristina Arrigoni,[1,8] Ahmed Rohaim,[1,7,8] David Shaya,[1] Felix Findeisen,[1] Richard A. Stein,[6] Shailika Reddy Nurva,[1] Smriti Mishra,[6] Hassane S. Mchaourab,[6] and Daniel L. Minor, Jr.[1,2,3,4,5,*]

[1]Cardiovascular Research Institute
[2]Department of Biochemistry and Biophysics
[3]Department of Cellular and Molecular Pharmacology
[4]California Institute for Quantitative Biomedical Research
University of California, San Francisco, San Francisco, CA 94158, USA
[5]Physical Biosciences Division, Lawrence Berkeley National Laboratory, Berkeley, CA 94720, USA
[6]Department of Molecular Physiology and Biophysics, Vanderbilt University, Nashville, TN 37232, USA
[7]Department of Biophysics, Faculty of Science, Cairo University, Giza, Egypt
[8]Co-first author
*Correspondence: daniel.minor@ucsf.edu
http://dx.doi.org/10.1016/j.cell.2016.02.001

SUMMARY

Voltage-gated ion channels (VGICs) are outfitted with diverse cytoplasmic domains that impact function. To examine how such elements may affect VGIC behavior, we addressed how the bacterial voltage-gated sodium channel ($BacNa_V$) C-terminal cytoplasmic domain (CTD) affects function. Our studies show that the $BacNa_V$ CTD exerts a profound influence on gating through a temperature-dependent unfolding transition in a discrete cytoplasmic domain, the neck domain, proximal to the pore. Structural and functional studies establish that the $BacNa_V$ CTD comprises a bi-partite four-helix bundle that bears an unusual hydrophilic core whose integrity is central to the unfolding mechanism and that couples directly to the channel activation gate. Together, our findings define a general principle for how the widespread four-helix bundle cytoplasmic domain architecture can control VGIC responses, uncover a mechanism underlying the diverse $BacNa_V$ voltage dependencies, and demonstrate that a discrete domain can encode the temperature-dependent response of a channel.

INTRODUCTION

Cells shape their electrical activity by controlling ion channel function in response to physical and chemical cues. Voltage-gated ion channels (VGICs) are exquisitely sensitive to transmembrane potential changes by virtue of a voltage-sensor domain that is embedded in the membrane bilayer (Vargas et al., 2012; Yu et al., 2005). Beyond the intrinsic ability to detect transmembrane voltage changes, VGIC superfamily members possess diverse intracellular domains (Yu et al., 2005) that are employed to tune voltage-dependent responses of a particular channel as a consequence of stimuli from signaling molecules (Morais-Cabral and Robertson, 2015; Yang et al., 2015). Although such domains provide a means for chemical cues to influence VGICs, the sensitivity to physical stimuli, such as temperature, in some VGIC superfamily members (Schneider et al., 2014; Vriens et al., 2014), has raised the question about whether there are equivalently specialized domains that can serve as temperature sensors (Bagriantsev et al., 2012; Brauchi et al., 2006; Grandl et al., 2008) or whether thermal responses arise from elements distributed throughout the channel (Chowdhury et al., 2014; Clapham and Miller, 2011). Moreover, despite notable advances in understanding the structures of some VGIC regulatory domains that respond to ligand or regulatory protein modulation (Jiang et al., 2002; Pioletti et al., 2006; Yuan et al., 2010; Zagotta et al., 2003), how conformational changes within these domains impact the channel pore and alter function remains incompletely understood.

Bacterial voltage-gated sodium channels ($BacNa_V$s) share the six-transmembrane VGIC superfamily architecture and bear a four-helix bundle C-terminal cytoplasmic domain (CTD) that terminates in a four-stranded coiled-coil (Irie et al., 2012; Mio et al., 2010; Payandeh and Minor, 2015; Powl et al., 2010; Shaya et al., 2014). $BacNa_V$s display remarkably diverse voltage responses (Payandeh and Minor, 2015; Scheuer, 2014), having activation potentials, $V_{1/2}$, that span an ~120 mV range (Scheuer, 2014), from −98 mV for Na_VAb from *Arcobacter butzleri* (Payandeh et al., 2012) to +27 mV for Na_VSp1 from *Silicibacter pomeroyi* (Shaya et al., 2014). The structural basis for this wide voltage response range is unknown (Scheuer, 2014). The CTD domain proximal to the channel pore termed the "neck" is the most diverse element (Payandeh and Minor, 2015; Powl et al., 2010; Shaya et al., 2014) and appears to adopt varied degrees of structure in different $BacNa_V$s (Bagnéris et al., 2013; Shaya et al., 2014; Tsai et al., 2013). Studies of different $BacNa_V$s indicate that the CTD is important for assembly (Bagnéris et al., 2013; Mio et al., 2010; Powl et al., 2010; Tsai et al., 2013) and function (Bagnéris et al., 2013; Irie et al., 2012; Shaya et al., 2014; Tsai et al., 2013). Nevertheless, a clear consensus for the mechanism by which the CTD influences channel function and the means by which it might influence the channel pore remains unknown.

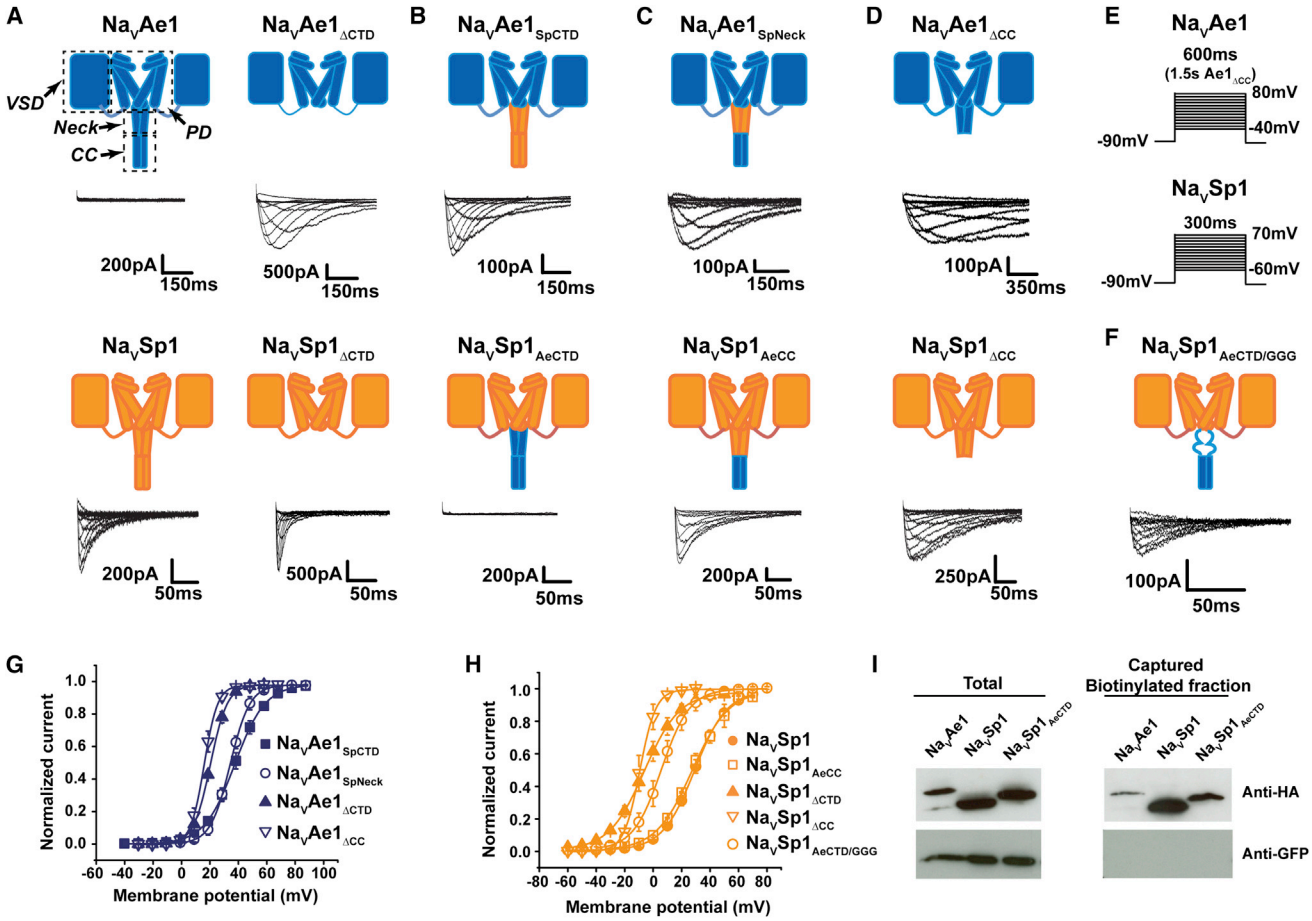

Figure 1. BacNa$_V$ CTD Affects Function

(A–D) Functional comparison of (A) Na$_V$Ae1, Na$_V$Sp1, Na$_V$Ae1$_{\Delta CTD}$, and Na$_V$Sp1$_{\Delta CTD}$; (B) Na$_V$Ae1$_{SpCTD}$ and Na$_V$Sp1$_{AeCTD}$; (C) Na$_V$Ae1$_{SpNeck}$ and Na$_V$Sp1$_{AeCC}$; and (D) Na$_V$Ae1 $_{\Delta CC}$ and Na$_V$Sp1 $_{\Delta CC}$. Cartoons depict two BacNa$_V$ subunits. Voltage-sensor domain (VSD), pore domain (PD), neck, and coiled-coil (CC) are labeled. Na$_V$Ae1 and Na$_V$Sp1 elements are blue and orange, respectively.

(E) Voltage protocols for Na$_V$Ae1 (top), Na$_V$Sp1 (bottom), and chimeras.

(F) Na$_V$Sp1$_{AeCTD/GGG}$ exemplar currents.

(G and H) Voltage-dependent activation curves for (G) Na$_V$Ae1, Na$_V$Ae1$_{SpCTD}$, Na$_V$Ae1$_{SpNeck}$, Na$_V$Ae1$_{\Delta CTD}$, and Na$_V$Ae1$_{\Delta CC}$, and (H) Na$_V$Sp1, Na$_V$Sp1$_{AeCC}$, Na$_V$Sp1$_{\Delta CTD}$, and Na$_V$Sp1$_{\Delta CC}$.

(I) Western blot of the total lysate and surface-biotinylated fraction for the indicated constructs probed using the specified antibodies.

See also Figure S1 and Table S1.

Here, we show that the BacNa$_V$ CTD has an integral role in controlling channel voltage-dependent behavior and that variation in neck composition and structure cause functional diversity. Moreover, we demonstrate that the neck has a temperature-dependent unfolding transition that is directly coupled to channel opening. These results establish that a discrete ion channel domain can serve as a temperature response element. The BacNa$_V$ CTD location is shared with many VGIC superfamily member helical bundle domains (Howard et al., 2007; Paulsen et al., 2015; Uysal et al., 2009; Wiener et al., 2008; Yu et al., 2012), including channels not principally gated by voltage. This architectural commonality suggests that the principles uncovered here set a framework for understanding how four-helix bundle CTDs can modulate VGIC superfamily member function.

RESULTS

BacNa$_V$ Cytosolic Domain Regulates Voltage-Dependent Channel Opening

To probe BacNa$_V$ CTD function, we focused on two BacNa$_V$s having different activation signatures, *Alkalilimnicola ehrlichii* Na$_V$Ae1 and *Silicibacter pomeroyi* Na$_V$Sp1. Na$_V$Sp1 displays robust voltage-dependent activity (Koishi et al., 2004; Shaya et al., 2014), whereas Na$_V$Ae1 has not yielded functional data unless neck mutations are present (Shaya et al., 2014) (Figure 1A). We deleted the Na$_V$Ae1 and Na$_V$Sp1 CTDs at the hinge between the pore module and CTD (ending at Na$_V$Ae1 His245 and Na$_V$Sp1 His224, respectively) (Figure S1A) (Shaya et al., 2014). Contrary to the loss of function reported for other BacNa$_V$ CTD deletions (Mio et al., 2010; Tsai et al., 2013), Na$_V$Ae1$_{\Delta CTD}$ and Na$_V$Sp1$_{\Delta CTD}$

produced robust voltage-dependent currents, demonstrating that CTD removal did not strongly affect folding or tetramerization (Figure 1A). However, CTD deletion had robust effects on voltage-dependent activation, causing large left shifts in $V_{1/2}$ relative to the references ($V_{1/2}$ = 19.1 ± 1.9 and 32.1 ± 1.1 mV, for $Na_VAe1_{\Delta CTD}$ and a functional mutant bearing a neck triple glycine substitution Na_VAe1_{GGG} [Shaya et al., 2014], respectively, and −7.4. ± 2.8 and 28.9 ± 1.3, for $Na_VSp1_{\Delta CTD}$ and Na_VSp1, respectively) (Figures 1G and 1H; Table S1). Thus, CTD deletion produces Na_VAe1 and Na_VSp1 channels that are more readily opened by voltage.

The CTD has two parts, the neck (Payandeh and Minor, 2015; Shaya et al., 2014), proximal to the transmembrane pore, and a C-terminal four stranded coiled-coil (Irie et al., 2012; Mio et al., 2010; Payandeh and Minor, 2015; Powl et al., 2010; Shaya et al., 2014). Because CTD deletion had such a strong effect on Na_VAe1 and Na_VSp1 function, we created a series of chimeras (Figure S1A) to define whether the effects caused by the CTD arise from the neck, coiled-coil, or both. CTD exchange between Na_VAe1 and Na_VSp1 yielded channels, Na_VAe1_{SpCTD} and Na_VSp1_{AeCTD}, that phenocopied the properties of the CTD parent; Na_VAe1_{SpCTD} was functional ($V_{1/2}$ = 38.8 ± 2.5 mV) whereas Na_VSp1_{AeCTD} showed no activity (Figure 1B; Table S1). Exchanging the Na_VAe1 coiled-coil into Na_VAe1_{SpCTD} to make an Na_VAe1 chimera bearing the Na_VSp1 neck and Na_VAe1 coiled-coil, Na_VAe1_{SpNeck}, produced a channel having voltage-dependent gating that was essentially identical to Na_VAe1_{SpCTD} ($V_{1/2}$ = 32.7 ± 2.0 and 38.8 ± 2.5 mV for Na_VAe1_{SpNeck} and Na_VAe1$_{SpCTD}$, respectively) (Figures 1C and 1G; Table S1). Substitution of the Na_VSp1 neck into Na_VSp1_{AeCTD} produced a Na_VSp1 chimera having the Na_VAe1 coiled-coil, Na_VSp1_{AeCC} that displayed voltage-dependent gating identical to Na_VSp1 ($V_{1/2}$ = 26.1 ± 1.0 and 28.9 ± 1.3 mV, for Na_VSp1_{AeCC} and Na_VSp1 respectively) (Figures 1C and 1H; Table S1). Taken together, these results demonstrate that coiled-coil identity has minimal functional effects, and the neck is the principal source of the differences in Na_VAe1 and Na_VSp1 voltage-dependent behaviors. Although the coiled-coil did not influence channel voltage-dependent properties, it seemed possible that its ability to constrain the neck C-terminal end might be important for the neck to affect gating. Therefore, we examined Na_VAe1 and Na_VSp1 mutants in which the neck was intact but the coiled-coil was deleted, $Na_VAe1_{\Delta CC}$ and $Na_VSp1_{\Delta CC}$. Both yielded channels having a $V_{1/2}$ indistinguishable from complete CTD deletion (19.1 ± 1.9 and 17.4 ± 1.7 mV for $Na_VAe1_{\Delta CC}$ and $Na_VAe1_{\Delta CTD}$; −7.4 ± 2.8 and −9.7 ± 1.9 mV for $Na_VSp1_{\Delta CC}$ and $Na_VSp1_{\Delta CC}$, respectively) (Figures 1D, 1G, and 1H; Table S1). Thus, together with the chimera results, these data indicate that the coiled-coil is required to constrain the C-terminal end of the neck, although its identity has minimal effect on function.

Because we were unable to measure currents from Na_VAe1 and Na_VSp1_{AeCTD} (Figures 1A and 1B), channels that have a wild-type Na_VAe1 neck, we tested whether these proteins had plasma membrane expression to resolve whether the lack of activity came from an absence of surface expression or from channels that could not be opened. We placed an N-terminal hemagglutinin (HA) tag on Na_VAe1, Na_VSp1_{AeCTD}, and Na_VSp1 and used a surface biotinylation assay to assess plasma membrane expression. Streptavidin capture of the surface-biotinylated fraction followed by anti-HA antibody detection showed clear signals for all three channels. By contrast, this fraction had no signal for the intracellular control, GFP, when probed with an anti-GFP antibody. Thus, the non-functional channels, Na_VAe1 and Na_VSp1_{AeCTD}, are indeed expressed on the plasma membrane (Figure 1I). Moreover, similar to the effects on Na_VAe1 (Shaya et al., 2014), inclusion of a triple-glycine substitution in the neck domain of Na_VSp1_{AeCTD} generated a functional channel ($Na_VSp1_{AeCTD/GGG}$ $V_{1/2}$ = 5.75 ± 2.6 mV; Figures 1F and 1H; Table S1). Together with the results of the chimeras and previous neck mutants (Shaya et al., 2014), these findings suggest that Na_VAe1 and Na_VSp1_{AeCTD} fail to produce currents because the Na_VAe1 neck produces a $V_{1/2}$ that is outside of the measureable voltage range of our experiments.

Our data demonstrate that the CTD functions as a regulatory module whose intrinsic properties enable it to exert diverse effects on $BacNa_V$ voltage-dependent gating. The neck influence is strong on voltage-dependent activation and contrasts with its modest effects on voltage-dependent inactivation (Figures 1, S1B, and S1C; Table S1), a process for which the pore domain is important (Pavlov et al., 2005; Payandeh et al., 2012; Shaya et al., 2014). Thus, our investigations establish that the origins of the dramatic modulation of voltage-dependent gating reside in the neck and require the neck to be constrained at the C-terminal end by the coiled-coil domain.

Diverse $BacNa_V$s CTDs Alter Na_VSp1 Transmembrane Domain Voltage Responses

Prior functional studies reported $BacNa_V$ $V_{1/2}$ activation values spanning an ~120 mV range (Koishi et al., 2004; Payandeh et al., 2012; Ren et al., 2001; Shaya et al., 2014; Ulmschneider et al., 2013). The source of this diversity has been unclear (Scheuer, 2014). Given the profound effects of the CTD on Na_VSp1 and Na_VAe1, we next asked how replacement of the Na_VSp1 CTD with CTDs from previously studied $BacNa_V$s having diverse lengths and compositions would affect function: Na_VBh1 (Na_VSp1_{BhCTD}), Na_VMs (Na_VSp1_{MsCTD}), Na_VAb (Na_VSp1_{AbCTD}), Na_VAb1 (Shaya et al., 2011) (Na_VSp1_{Ab1CTD}), and Na_VPz (Na_VSp1_{PzCTD}) (Figures 2A and S1A). In whole cell recordings, each of these channels, except Na_VSp1_{AbCTD}, was functional (Figure 2B). Strikingly, the CTD substitutions had diverse effects ranging from little change in voltage-dependent activation relative to Na_VSp1 for the Na_VPz CTD ($\Delta V_{1/2}$ = −4.2 mV) to producing large voltage-dependent activation shifts in both the negative ($\Delta V_{1/2}$ = −44.5 ± 4.4 and −27.3 ± 3.8 mV, Na_VBh1 and Na_VMs CTDs, respectively) and positive directions ($\Delta V_{1/2}$ = +20.4 ± 5.8 mV Na_VAb1 CTD) (Figure 2C; Table S1). For the Na_VSp1_{BhCTD}, the activation threshold was similar to that of $Na_VSp1_{\Delta CTD}$ ($\Delta V_{1/2}$ = −44.5 ± 4.4 mV and −36.3 ± 5.4 mV, respectively), a result that is in line with data suggesting that the Na_VBh1 neck is disordered (Powl et al., 2010) and the observation that Na_VBh1 coiled-coil deletion results in channels having voltage-dependent activation indistinguishable from wild-type (Mio et al., 2010). By contrast, the CTD swaps had a more modest effect on voltage-dependent inactivation (Figure S1D; Table S1).

The varied effects of the different CTD chimeras on the voltage-dependence of the Na_VSp1 transmembrane core demonstrate

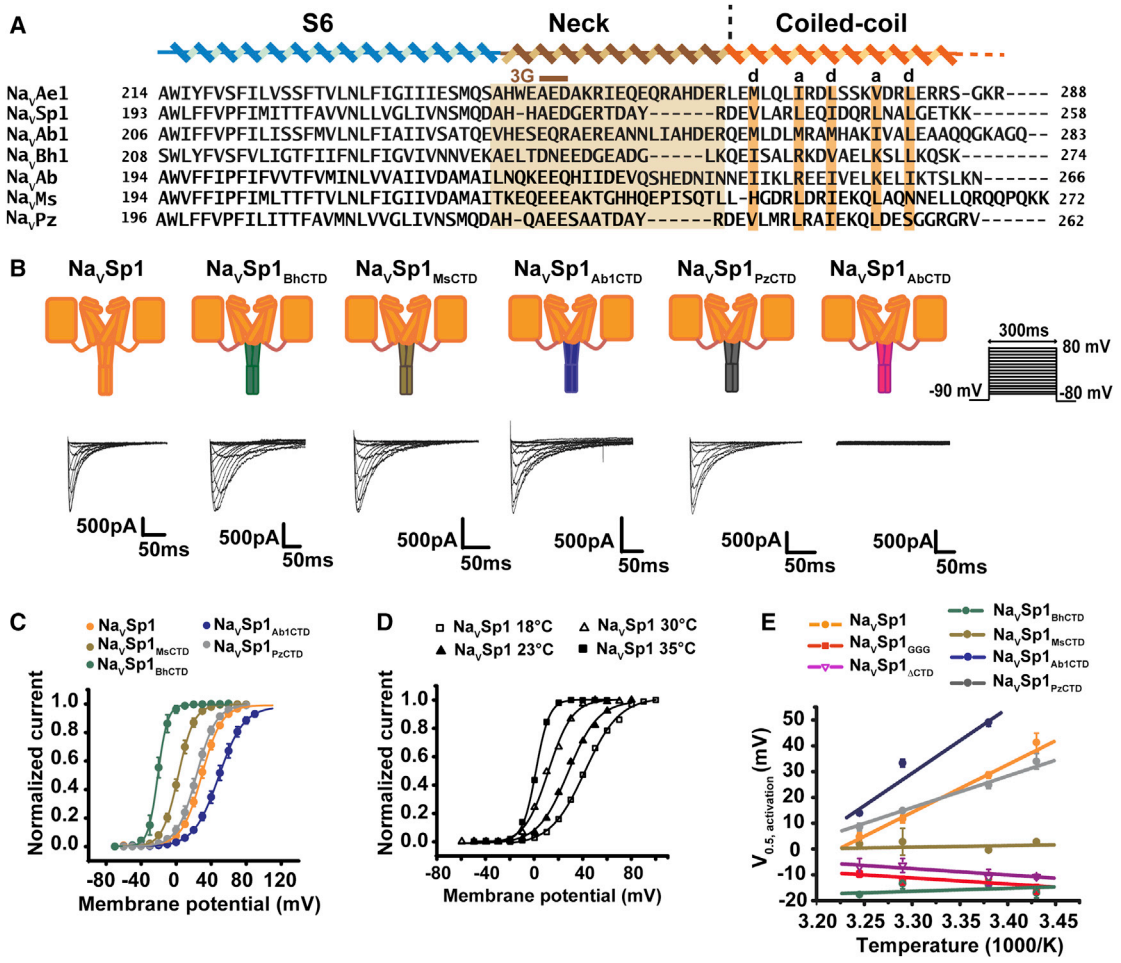

Figure 2. CTD Chimeras Alter Na_VSp1 Voltage-Dependence

(A) Sequence alignment of Na_VAe1, *Alkalilimnicola ehrlichii* (Shaya et al., 2011, 2014), Na_VSp1, *Silicibacter pomeroyi* (Koishi et al., 2004; Shaya et al., 2011); Na_VAb1, *Alcanivorax borkumensis* (Shaya et al., 2011); Na_VBh1 (NaChBac), *Bacillus halodurans* (Ren et al., 2001); Na_VAb, *Arcobacter butzleri* (Payandeh et al., 2011); Na_VMs, *Magnetococcus sp*. (McCusker et al., 2012); and Na_VPz, *Paracoccus zeaxanthinifaciens* (Koishi et al., 2004). S6, neck, coiled-coil "a"-"d" positions, and 3G mutation site are indicated.

(B) NaSp1, Na_VSp1_{BhCTD}, Na_VSp1_{MsCTD}, Na_VSp1_{Ab1CTD}, Na_VSp1_{PzCTD}, and Na_VSp1_{AbCTD} exemplar currents and voltage protocol. Cartoons depict two channel subunits.

(C) Activation curves for (B).

(D) Temperature-dependence of Na_VSp1 activation.

(E) $V_{1/2}$ temperature-dependence for the indicated channels. Lines show linear fit.

See also Figures S1 and S2 and Tables S1 and S2.

that each $BacNa_V$ CTD has a distinct effect on channel activation (Figure 2B) and that a simple $BacNa_V$ CTD transplant can tune the voltage-dependence of activation of the transmembrane core over a wide range, ~65 mV (Figure 2C). These results, taken together with the experiments indicating the clear involvement of the $BacNa_V$ neck in channel function (Figure 1) and lack of sensitivity to coiled-coil identity (Figure 1C), strongly support a critical role for the neck in $BacNa_V$ gating. Although specific elements of the $BacNa_V$ transmembrane domains, such as the voltage sensors, must set some of the channel voltage-dependent properties, our findings together with the observation that the neck is the most variable $BacNa_V$ feature (Payandeh and Minor, 2015), indicate that much of the observed variety in $BacNa_V$ voltage-dependences originates from the neck region. These domains display varied degrees of structure from disordered (Bagnéris et al., 2013; Powl et al., 2010) to completely ordered (Shaya et al., 2014). Thus, our data points to a common mechanism for tuning voltage dependencies within the $BacNa_V$ family based on the ability of the neck to adopt structure.

Temperature-Dependent Change in the $BacNa_V$ Neck Affects Gating

Previous studies suggested that the neck undergoes an order → disorder transition during channel opening (Shaya et al., 2014)

and pose a hypothesis that predicts very different temperature dependences for BacNa$_V$s in which the neck is stably folded structure versus those in which it is disordered. To test this, we first examined whether Na$_V$Sp1 voltage-dependent activation was temperature-dependent and whether this response could be influenced by neck properties. The $V_{1/2}$ of Na$_V$Sp1 activation showed a clear temperature dependence, moving ~35 mV in the hyperpolarized direction as temperature increased from 18° to 35°C (Figures 2D and 2E; Table S2). This response was eliminated by increasing the neck flexibility with a triple glycine substitution, Na$_V$Sp1$_{GGG}$ (Shaya et al., 2014), or by CTD deletion, Na$_V$Sp1$_{\Delta CTD}$ (Figure 2E; Table S2), supporting the idea that neck structure is crucial for temperature-dependent gating changes.

Because the Na$_V$Sp1 CTD chimeras displayed diverse activation $V_{1/2}$ values (Figure 2C), we next probed whether these CTD substitutions affected channel temperature responses. The chimeras having CTDs bearing disordered necks, Na$_V$Sp1$_{BhCTD}$ and Na$_V$Sp1$_{MsCTD}$ (Bagnéris et al., 2013; Powl et al., 2010), yielded channels that lacked a temperature response in activation $V_{1/2}$ (Figure 2E; Table S2). By contrast, the activation $V_{1/2}$ of Na$_V$Sp1$_{PzCTD}$ and Na$_V$Sp1$_{Ab1CTD}$ showed clear temperature dependence. This response was similar in magnitude to Na$_V$Sp1 (Figure 2E) and shows that the role of the CTD in setting channel temperature-dependent properties is general.

Finally, we examined whether the $V_{1/2}$ changes caused by the CTD substitutions were related to neck structure by examining the consequences of neck triple glycine mutations in Na$_V$Sp1$_{MsCTD}$, Na$_V$Sp1$_{Ab1CTD}$, and Na$_V$Sp1$_{PzCTD}$ (Figures S2A and S2B). Neck disruption had no effect on the activation $V_{1/2}$ for the chimera having a disordered neck, Na$_V$Sp1$_{MsCTD}$ ($\Delta V_{1/2}$ = 0.9 mV Na$_V$Sp1$_{MsCTD/GGG}$ relative to Na$_V$Sp1$_{MsCTD}$) (Figure S2C; Table S1). However, for both chimeras having a temperature-dependent $V_{1/2}$ similar to Na$_V$Sp1, Na$_V$Sp1$_{PzCTD}$ and Na$_V$Sp1$_{Ab1CTD}$, the GGG mutation caused a large activation $V_{1/2}$ left-shift ($\Delta V_{1/2}$ = −39.3 and −47.2 mV, respectively, for Na$_V$Sp1$_{PzCTD}$ and Na$_V$Sp1$_{Ab1CTD}$, relative to the parent chimeras) (Figures S2D and S2E; Table S1). This magnitude change is similar to that in Na$_V$Sp1$_{GGG}$ ($\Delta V_{1/2}$ = −39.4 mV) (Figure S2F; Table S1). Given that the triple glycine mutation eliminates Na$_V$Sp1 temperature-dependence, these data suggest that the modulatory effects on $V_{1/2}$ and the temperature-dependent gating properties in Na$_V$Sp1$_{PzCTD}$ and Na$_V$Sp1$_{Ab1CTD}$ arise from neck domain order. Taken together, our data strongly support the hypothesis that a protein unfolding transition in the neck domain is coupled to channel opening and demonstrate that a discrete channel domain can act as a temperature sensor.

Structures of Na$_V$Ae1p Neck Mutants Reveal Disordered Neck and Closed Pore

To define the structural consequences of polyglycine mutations intended to disrupt the neck, we determined crystal structures of two neck domain mutants of "pore-only" channel Na$_V$Ae1p (Shaya et al., 2014), Na$_V$Ae1p-3G and Na$_V$Ae1p-7G, at 3.70 Å and 3.80 Å resolution, respectively (Figures 3A–3D and S3; Table S3). Molecular replacement using the Na$_V$Ae1p transmembrane portion (Shaya et al., 2014) yielded maps having well-defined electron density for the transmembrane regions and part of the CTDs (Figures S4A and S4B). Model building and refinement showed traceable density for residues that comprise the neck C-terminal ends and complete coiled-coils (Na$_V$Ae1p-3G Ile254-Arg283 and Na$_V$Ae1p-7G Glu257-Arg283) (Figures 3A and 3B) but lacked density for the polyglycines and residues that frame these substitutions (Na$_V$Ae1p-3G Ser243-Arg253 and Na$_V$Ae1p-7G Ser243-Gln256). This localized loss of structure confirms the increase in neck flexibility and shows that the disruption propagates beyond the polyglycines (Figure 3D).

Although the Na$_V$Ae1p-3G and Na$_V$Ae1p-7G necks lack structure, both CTD coiled-coils remained intact. These were displaced from the channel central axis by ~28° (Figure 3C) and in agreement with its increased disorder, this displacement was larger for Na$_V$Ae1p-7G and included a ~8 Å movement toward the pore (Figure 3C). Once the neck is disrupted, the pore domain and coiled-coil appear to be independent. We anticipate that free from the crystal lattice constraints, the coiled-coil could move independently relative to the pore as solution studies suggest (Bagnéris et al., 2013). The fact that the neck disruption does not propagate into the coiled-coil agrees with our observation that coiled-coil identity is not crucial for function but that its presence is essential for the neck to affect function (Figures 1C and 1D).

Although the 3G and 7G substitutions make full-length BacNa$_V$s easier to open, Na$_V$Ae1p-3G and Na$_V$Ae1p-7G pore domains are closed and match the Na$_V$Ae1p closed structure (Figure S4C) (Shaya et al., 2014) (root-mean-square deviation $[RMSD]_{C\alpha}$ of 0.67 Å and 0.73 Å, respectively). Assignment of a closed conformation is further supported by anomalous difference maps of selenomethionine substituted Na$_V$Ae1p-3G (Figure S4D; Table S3) that reveal clear density on the pore domain central axis for the seleniums of the activation gate residue, Met241 (Shaya et al., 2014). Na$_V$Ae1p-3G and Na$_V$Ae1p-7G structures also revealed density in the selectivity filter "site 2" position (Tang et al., 2014) (Figures S4E–S4G) that we modeled as a calcium atom based on anomalous density (Figure S4F) and the presence of calcium in the crystallization conditions.

As there is no structure of Na$_V$Sp1 or the "pore-only" Na$_V$Sp1p (Shaya et al., 2011), we turned to circular dichroism (CD) spectroscopy to test whether the Na$_V$Ae1p-3G and Na$_V$Ae1p-7G structural changes had parallels in Na$_V$Sp1p. Na$_V$Ae1p, Na$_V$Ae1p-3G, and Na$_V$Ae1p-7G CD spectra showed classic helical features of minima at 208 and 222 nm (Berova et al., 2000). Notably, the intensity of these minima was reduced in Na$_V$Ae1p-3G and Na$_V$Ae1p-7G in an order that matched the crystal structures and was reduced farther by CTD deletion in Na$_V$Ae1p-ΔCTD (Figure 3E). Comparison of the CD spectra of Na$_V$Sp1p (Shaya et al., 2011) with Na$_V$Sp1p-3G showed a similar loss of helical structure (Figures 3D and 3F). To test whether neck disruption affected the thermal stability, we measured the temperature dependence of the CD signal at 222 nm. The data show that in Na$_V$Ae1p introduction of neck region glycines increases the thermal liability of the measured transition following the rank order as expected from the crystal structures (Na$_V$Ae1p > Na$_V$Aep1-3G > Na$_V$Ae1p-7G) (Figure 3G). Notably, Na$_V$Ae1p-ΔCTD lacks a cooperative thermal transition, demonstrating that the measured changes in thermal behavior arise from the CTD (Figure 3G). Further, Na$_V$Sp1p is less stable than

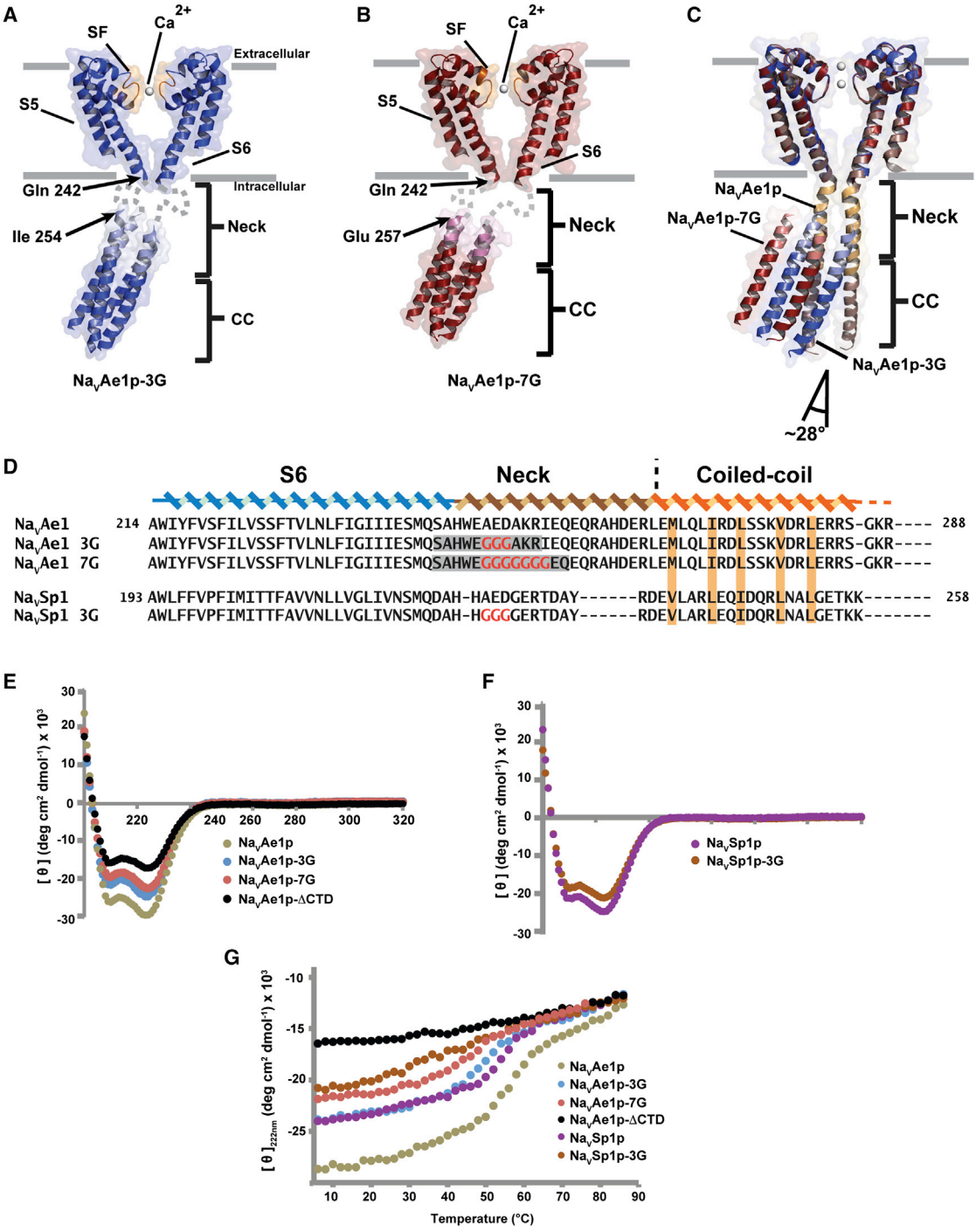

Figure 3. BacNa$_V$ Neck Disruption Structural Outcomes

(A and B) Cartoons of two subunits of (A) Na$_V$Ae1p-3G (dark blue) and (B) Na$_V$Ae1p-7G (firebrick) structures. Grey dashes indicate regions lacking electron density. Residues defining the electron density limits are indicated. Selectivity filter is orange.

(C) Superposition of Na$_V$Ae1p (orange) (Shaya et al., 2014), Na$_V$Ae1p-3G (dark blue), and Na$_V$Ae1p-7G (firebrick). Angle shows Na$_V$Ae1p-7G coiled-coil displacement. Selectivity filter ion positions are shown.

(D) S6-CTD sequences for the indicated channels. Polyglycine positions are red. Regions lacking electron density are gray. Coiled-coil "a-d" repeat is orange.

(E and F) CD spectra for the indicated proteins at 4°C.

(G) Thermal denaturation curves for the indicated proteins.

See also Figures S3 and S4 and Table S3.

Na_VAe1p and the introduction of the triple glycine neck mutant in Na_VSp1p eliminated the thermal transition, in agreement with the function of the parent channels (Figures 1 and 2). Together, the crystallographic and CD data demonstrate that increasing $BacNa_V$ neck flexibility leads to a loss of structure that is restricted to the neck, show that these changes increase the neck thermal sensitivity, and indicate that this disruption is the source of the functional changes caused by polyglycine substitution.

Electron Paramagnetic Resonance Spectroscopy Reveals Changes in Neck Dynamics

To investigate the CTD domain dynamics, we used site-specific spin labeling with the nitroxide spin probe (1-Oxyl-2,2,5,5-tetramethylpyrroline-3-methyl) methanethiosulfonate (MTSSL) and electron paramagnetic resonance (EPR) studies (Mchaourab et al., 2011). We probed select positions on the exterior of the Na_VAe1p and Na_VAe1p-3G CTDs by labeling three neck sites (Glu247 and Ala251 that frame polyglycine sites in Na_VAe1p-3G and Glu255 at the beginning of the Na_VAe1p-3G ordered region) (Figures 3A and 4A), three coiled-coil sites (Glu266, Gln269, and Asp273), and a site at the protein C terminus (Arg283) (Figure 4A). Double electron-electron resonance (DEER) spectroscopy indicated that, with the exception of Arg283, the probe positions in Na_VAe1p have spin echo decays with a well-defined oscillation (Figure 4B). The corresponding distance distributions match those expected from the structure (~25 Å and ~35 Å for adjacent and diagonal nitroxide positions, respectively). By contrast, introduction of triple glycine at residues 248–250 (Figure 4A) caused clear changes at Glu247 and Ala251. These decays showed evidence of superimposed longer component that is manifested in the distance distributions. We interpret this component as indicative of increased disorder (Figure 4B). Notably, minimal changes occurred at Glu255, in complete agreement with the order seen at this site in the crystal structure (Figure 3A). Further, no differences were observed at any coiled-coil positions. Thus, these data reinforce the view from our crystallographic studies that introduction of polyglycine sequences into the neck increase its mobility and spare the coiled-coil structure.

There are clear functional differences between Na_VAe1 and Na_VSp1 that originate in the CTD (Figure 1). Therefore, we probed Na_VSp1p at positions equivalent to those tested in Na_VAe1p and Na_VAe1p-3G (Figure S5) to see whether there was a structural correlate underlying the diverse functional properties. Na_VSp1p continuous wave (CW) and DEER studies reveal notable differences in the dynamics of the neck versus the coiled-coil. By contrast to Na_VAe1p, the Na_VSp1p neck positions consistently display DEER decays that have a longer distance component, similar to those in Na_VAe1p-3G, whereas the Na_VSp1p coiled-coiled DEER signals resemble what is observed in Na_VAe1p (Figure S5B). These differences between EPR probe mobility in the neck and coiled-coil is similar to those observed in Na_VMs (Bagnéris et al., 2013). Importantly, our data strongly support the notion from the chimera (Figure 2) and CD experiments (Figure 3G) that the neck domains of different $BacNa_VS$ have diverse degrees of inherent order and that these differences are the origins of functional diversity.

Na_VAe1p Neck Has a Hydrophilic Core and a π-Stack Structure Important for Gating

In parallel with our studies of Na_VAe1p mutants, we obtained Na_VAe1p crystals that diffracted to superior resolution than previously reported (Shaya et al., 2014) (2.95Å versus 3.46Å, respectively) (Figures S6A and S6B; Table S3). Although the overall architecture is unchanged (Figure S6C), the increased resolution revealed previously uncharacterized CTD features. Notably, there is a striking bipartite organization in the core of the CTD neck and coiled-coil domains. The coiled-coil core follows the classic heptad repeat "a-d" packing (Lupas and Gruber, 2005) (Figures 5A–5C) and comprises five layers of hydrophobic residues (Met267, Ile271, Leu274, Val278, and Leu281) and a terminal, more open layer at Ser285 (Figures 5B and 5C). By contrast, the neck core is composed almost exclusively of hydrophilic side chains. These also follow a heptad pattern but include a one residue skip at the Gln256-Gln257 junction (Figure 5A). Consistent with the splaying of the neck helices (Shaya et al., 2014), the neck has a less well-packed core than the coiled-coil (Figures 5B and 5C). The stark differences between the structures and compositions of the neck and coiled-coil cores suggest that the neck is metastable and provide an explanation for why it is able to change structure during channel gating.

The 2.95 Å resolution Na_VAe1p structure revealed a number of interesting non-protein entities associated with the channel. There are two ions in the CTD core. One is at the N-terminal end of the neck, the "neck ion" (Shaya et al., 2014), and a second is at the neck/coiled-coil junction, the "coiled-coil ion" (Figure 5B). Data collected at the bromine absorption edge from Na_VAe1p crystals grown in 200 mM NaBr and soaked in cryoprotectant solutions containing 200 mM or 0 mM NaBr showed strong anomalous densities for both ions in 200 mM NaBr, but only for the coiled-coil ion in 0 mM NaBr (Figure S6D), demonstrating that both CTD ions are halogens and that the neck ion is labile. Based on these observations and the presence of chloride in the 2.95 Å structure crystallization conditions, we modeled both ions as chloride (Figure S6E). The selectivity filter has density corresponding to two sodium ions bridged by a water molecule. One sodium ion occupies the level of the Glu197 sidechain (corresponding to "site 2") (Tang et al., 2014), and the second is found at the level of Thr195 ("site 3") (Figure S6F). We also identified a number of lipids including one occupying a site observed in a number of other $BacNa_V$ structures (Payandeh and Minor, 2015) that is located next to the P1 pore helix and wedged between the subunits (Figure S6G).

The neck ion binding site arises from an unusual motif, the "π-stack," in which Trp246 from one subunit makes a face-to-face stacking interaction with His245 from the neighbor (Figures 5B–5E) and creates a neck ion binding site coordinated by the Trp246 indole nitrogens. The coiled-coil ion binding site comprises successive "a-d-a" positions in the CTD core (Figures 5B, 5C, and 5F). Four guanido moieties from Arg264 that occupy the first 'a' position of the coiled-coil "a-d" repeat coordinate the halide ion (Figure 5F). This ionic complex forms an "electrostatic pin" in the helical bundle core. The Arg264 sidechains extend into the space that should be occupied by the preceding "d" side chains of the neck core. The presence of a small residue

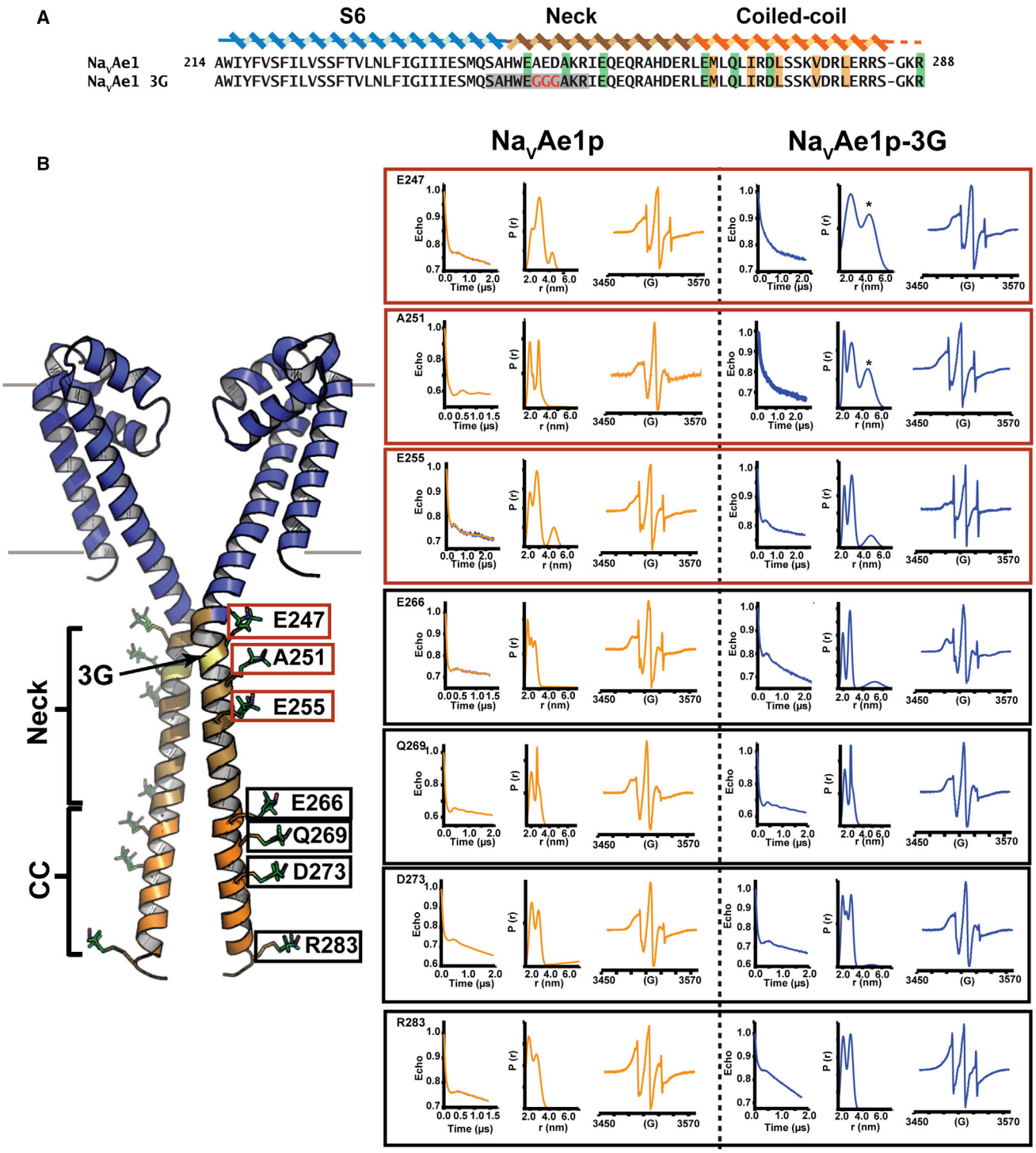

Figure 4. Na_VAe1p EPR Studies

(A) S6-CTD region sequences. Spin label positions, polyglycine substitutions and, Coiled-coil "a"-"d" repeat are highlighted green, red, and orange, respectively. Na_VAe1p-3G residues lacking electron density are gray.

(B) Na_VAe1p cartoon of two subunits and spin label sites. Pore domain, neck, and coiled-coil are slate, sand, and orange, respectively, Red and black boxes denote neck and coiled-coil spin-label positions, respectively. Panels show DEER decays, distance distributions, and CW spectra. Asterisks indicate the new Na_VAe1p-3G long-range distances.

See also Figure S5.

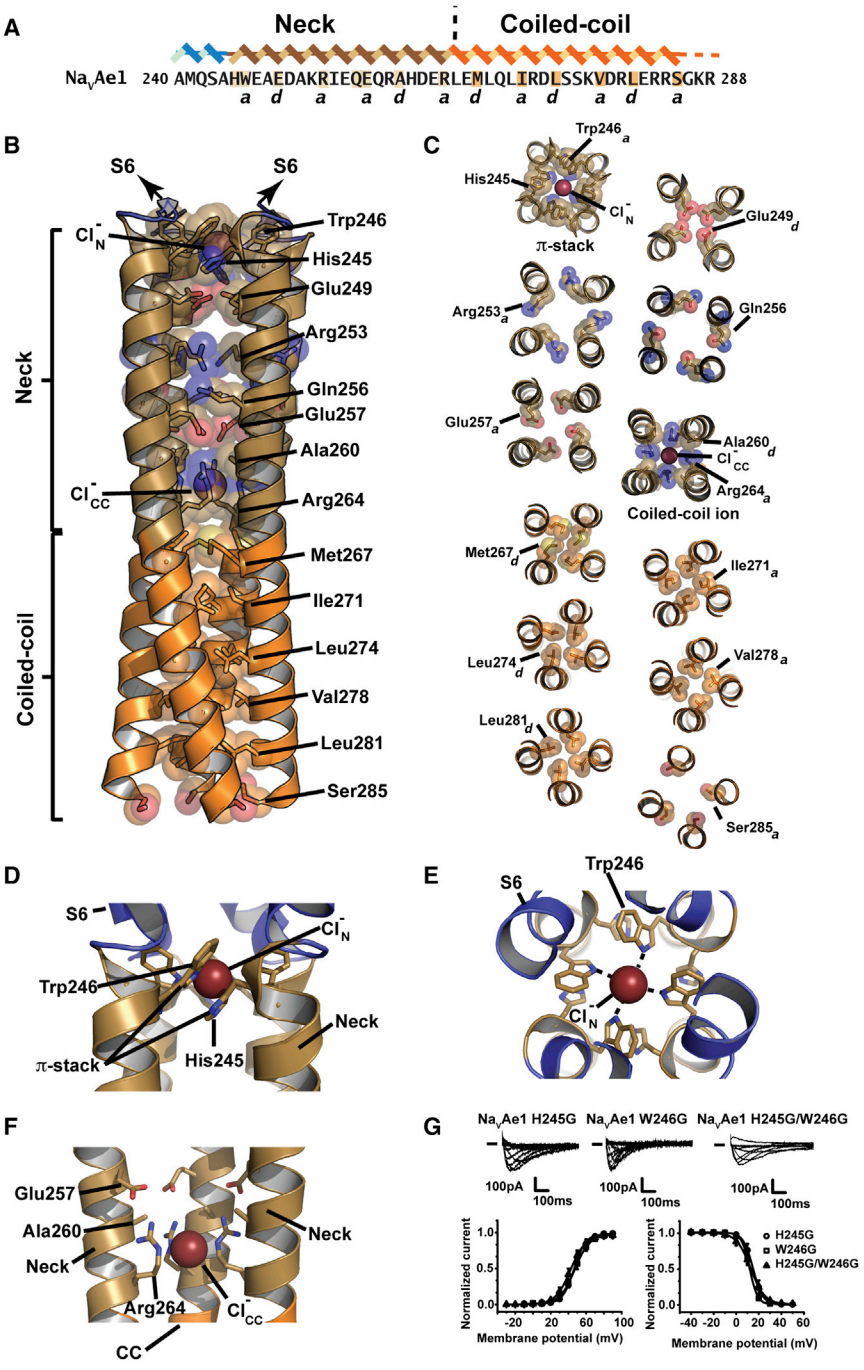

Figure 5. Na_VAe1p CTD Structure

(A) Na_VAe1 sequence. Neck and coiled-coil "a"-"d" core residues, His245, and Glu256 are highlighted.

(B) Na_VAe1p CTD cartoon showing core residues. Neck ion, Cl^-_N, and Coiled-coil ion, Cl^-_{CC} are indicated. S6, neck, and coiled-coil are slate, sand, and orange, respectively.

(C) Na_VAe1p CTD π-stack, "a" and "d" layers, and Coiled-coil ion site packing geometries.

(D and E) π-stack ion binding site (D) side and (E) top views. His245, Trp246, and Neck ion, Cl^-_N, are indicated.

(F) Coiled–coil ion binding site. Glu257, Ala260, Arg264, and coiled-coil ion, Cl^-_{CC} are indicated.

(G) Na_VAe1_{H245G}, Na_VAe1_{W246G}, and $Na_VAe1_{H245G/W246G}$ exemplar currents and voltage-dependence of activation and inactivation. Colors are as in Figure 4.

See also Figures S6 and S7 and Table S3.

at this position, Ala260, accommodates the Arg264 guanido moieties and permits them to interact with the Glu257 carboxylates from the "a" position above (Figures 5C and 5F). Interestingly, the "electrostatic pin" formed by the coiled-coil ion binding site marks where the CTD helices diverge from the canonical coiled-coil packing. Further, in the Na_VAe1p-3G and Na_VAe1p-7G structures, disruption of the helical structure propagates through the π-stack but stops at the coiled-coil ion binding site (Figure S6E). These observations agree with the apparent binding differences in the neck and coiled-coil ions and the metastable nature of the neck hydrophilic core versus the stable coiled-coil hydrophobic core. π-stack and coiled-coil ion motifs signatures occur in other $BacNa_V$ sequences and indicate that these structures are present in other channels (Figure S7).

Because the Na_VAe1p-3G and Na_VAe1p-7G structures showed disrupted π-stack elements due to the polyglycine mutations (Figures 3A, 3B, 3D, and S6E), we wanted to test whether direct disruption of this structural element would affect function. As with other Na_VAe1 neck destabilizing mutations (Shaya et al., 2014), mutation of either π-stack residue to glycine resulted in measurable currents (Figure 5G). As expected from the intersubunit stacking, $Na_VAe1_{H245G/W246G}$ had essentially identical voltage-dependent activation and inactivation properties compared to Na_VAe1_{H245G} and Na_VAe1_{W246G}, demonstrating that the two π-stack elements are co-dependent (Figure 5G; Table S1). A previous Na_VAe1p_{H245G} low resolution structure showed that π-stack disruption leads to neck ion loss but little perturbation to the neck helix (Shaya et al., 2014). Thus, the π-stack architecture serves as a type of lock in the Na_VAe1 neck to oppose channel opening.

$BacNa_V$ Neck Is Energetically Coupled to the Channel Gate

Does the $BacNa_V$ neck affect function by impacting the channel gate, the voltage sensors, or both? To answer this question, we pursued a double mutant cycle strategy (DeCaen et al., 2009;

Yifrach and MacKinnon, 2002) examining whether disruption of the Na_VSp1 neck by the GGG substitution, Na_VSp1_{GGG}, had additive or non-additive effects on voltage gating when placed in the context of mutations that perturb the gate or the voltage sensors. To test whether the neck and gate are coupled, we compared the properties of the Na_VSp1 channel gate mutant, Na_VSp1_{M220A} (Shaya et al., 2014), Na_VSp1_{GGG}, and a channel bearing both mutations $Na_VSp1_{M220A/GGG}$ (Figures 6A and 6B). To probe for coupling to the voltage sensors, we neutralized each of the four arginines at $BacNa_V$ S4 voltage sensor positions R1–R4 (Payandeh et al., 2011; Zhang et al., 2012) by mutation to glutamine (Figure 6C) in order to perturb the ease of voltage sensor movement and measured the properties of Na_VSp1_{R1Q}, Na_VSp1_{R2Q}, Na_VSp1_{R3Q}, and Na_VSp1_{R4Q}, alone and in combination with the GGG neck mutation (Figures 6D and 6E).

As observed previously, gate destabilization, Na_VSp1_{M220A} (Shaya et al., 2014), and neck disruption, Na_VSp1_{GGG} (Shaya et al., 2014), caused substantial leftward shifts in the activation $V_{1/2}$ (27.7 ± 1.6 mV, −10.5 ± 2.1 mV, and −18.6 ± 2.7 mV for $V_{1/2}$ of Na_VSp1, Na_VSp1_{GGG}, and Na_VSp1_{M220A}, respectively) (Figure 6B; Table S4). Combining both, $Na_VSp1_{M220A/GGG}$, resulted in a $V_{1/2}$ left shift beyond that of the individual changes (−28.3 ± 4.0 mV) (Figure 6B; Table S4). R1 neutralization did not affect the activation $V_{1/2}$ (31.1 ± 1.2 mV), whereas other arginine position neutralizations shifted the activation $V_{1/2}$ in either the positive (Na_VSp1_{R2Q} and Na_VSp1_{R4Q}, 44.8 ± 2.1 mV and 59.9 ± 3.2 mV, respectively) or negative (Na_VSp1_{R3Q}, 11.7 ± 2.3 mV) directions relative to Na_VSp1 (Figure 6E; Table S4). In each case, combination with GGG neck mutation caused a substantial left shift in $V_{1/2}$ (Figure 6E) ($Na_VSp1_{R1Q/GGG}$, $Na_VSp1_{R2Q/GGG}$, $Na_VSp1_{R3Q/GGG}$, and $Na_VSp1_{R4Q/GGG}$, −9.2 ± 1.9 mV, 44.8 ± 2.1 mV, −24.5 ± 1.8 mV, and 32.7 ± 2.0 mV, respectively).

By taking changes in $V_{1/2}$, estimated gating charge, $Z(e_0)$, and slope factor (k) (DeCaen et al., 2009; Yifrach and MacKinnon, 2002), we determined the activation-free energy at 0 mV. Comparison of measured double mutant-free energy perturbations relative to Na_VSp1 ($\Delta\Delta G^\circ_{obs}$) with values calculated additive effects of individual mutants ($\Delta\Delta G^\circ_{calc}$) revealed a clear contrast between how neck perturbation affects the pore and voltage sensors (Table S4). $\Delta\Delta G^\circ_{obs}$ for the neck-gate combination, $Na_VSp1_{M220A/GGG}$, −3.1 kcal mol^{-1}, is substantially less than that expected from the individual changes ($\Delta\Delta G^\circ_{calc}$ = −5.0 kcal mol^{-1}) (Table S4). By contrast, $\Delta\Delta G^\circ_{obs} = \Delta\Delta G^\circ_{calc}$ for all neck-voltage sensor pairs (Table S4). Thus, these data indicate that the neck affects gating voltage dependence by direct perturbation of the channel gate. Given its location and the importance of neck structure, such an effect must come from the ability of the neck to constrain pore opening.

DISCUSSION

VGIC cytosolic domains are important channel modulation loci. Hence, there is a great interest in understanding how their structural transformations affect VGIC transmembrane channel core. The simple $BacNa_V$ CTD architecture, comprising four parallel helices, provides an elegant paradigm for defining how VGIC CTDs can influence channel gating. Our studies of $BacNa_V$ CTDs reveal a VGIC modulation mechanism built on the bipartite architecture of the $BacNa_V$ CTD four-helix bundle. The key feature, the neck domain, is a membrane proximal four-helix bundle bearing a hydrophilic core that forms a metastable structure. This domain is constrained on its N and C termini by the channel pore domain and a classic parallel four-stranded coiled-coil, respectively. These physical constraints are essential for the neck to influence voltage-dependent gating and their importance is supported by two key observations: (1) deletions of the entire CTD (Figures 1G and 1H; Table S1) shift the voltage-dependent gating in the hyperpolarized direction in a manner equivalent to deletion of only the coiled-coil (Figure 1; Table S1), and (2) mutant cycle analysis shows strong energetic coupling between the activation gate of the channel pore and the neck (Figure 6; Table S4).

The origin of the wide range of $BacNa_V$ voltage-dependent activation responses has been unclear (Scheuer, 2014). The diverse and largely hydrophilic nature of $BacNa_V$ neck domains contrasts with the well-conserved CTD coiled-coil and high conservation of key voltage sensor domain elements (Payandeh and Minor, 2015). This neck sequence diversity, together with the capacity of different $BacNa_V$ CTDs to tune voltage-responses of the Na_VSp1 transmembrane core by >65 mV (Figures 2A–2C), indicates that even though features of the transmembrane domains are likely to set some voltage-depending gating properties, much of the varied voltage responses among $BacNa_V$s arises from differences in neck domain properties. These gating effects are directly correlated with the ability of the neck to adopt a stable structure. Studies of chimeras containing the Na_VSp1 transmembrane domain and CTDs from other $BacNa_V$s show that channels having the Na_VBh1 neck, which is disordered (Powl et al., 2010), have a voltage sensitivity that is equivalent to those lacking the entire CTD (Figures 1H and 2C), whereas those having a completely ordered CTD, Na_VAe1 (Shaya et al., 2014), require stronger depolarizations to open. Further, structural and functional studies show that increased neck disorder shifts the activation of both Na_VAe1 and Na_VSp1 to more hyperpolarized potentials (Figure 3) (Shaya et al., 2014). In this regard, our discovery of the "π-stack" halogen-binding site (Figures 5D and 5E) provides a clear explanation for why Na_VAe1, among all other $BacNa_V$s, can only be opened if the neck is destabilized.

Previous deletion studies of different $BacNa_V$s reported varied effects, including a left shift in voltage-dependent activation for Na_VSulP (Irie et al., 2012) and no change for Na_VBh1 (Mio et al., 2010), and provided no clear view of why there were different outcomes in different channel contexts. Our data now point to a unified mechanism for $BacNa_V$ gating in which the CTDs tune the ease of voltage-dependent opening of the channel based on the propensity of the neck region to adopt an ordered state. Due to its high polar residue content, the neck structure is metastable and contrasts with the stable hydrophobic core of the terminal coiled coil. This property is critical for the neck to undergo the order → disorder transition associated with channel opening (Figure 7A). Although CTD mutations can impact channel inactivation properties (Figures S1B–S1D) (Bagnéris et al., 2013; Irie et al., 2010, 2012; Tsai et al., 2013), the effects are diverse in different $BacNa_V$s and likely reflect a complex inactivation process that also involves key contributions from elements of the pore domain (Pavlov et al., 2005; Payandeh et al.,

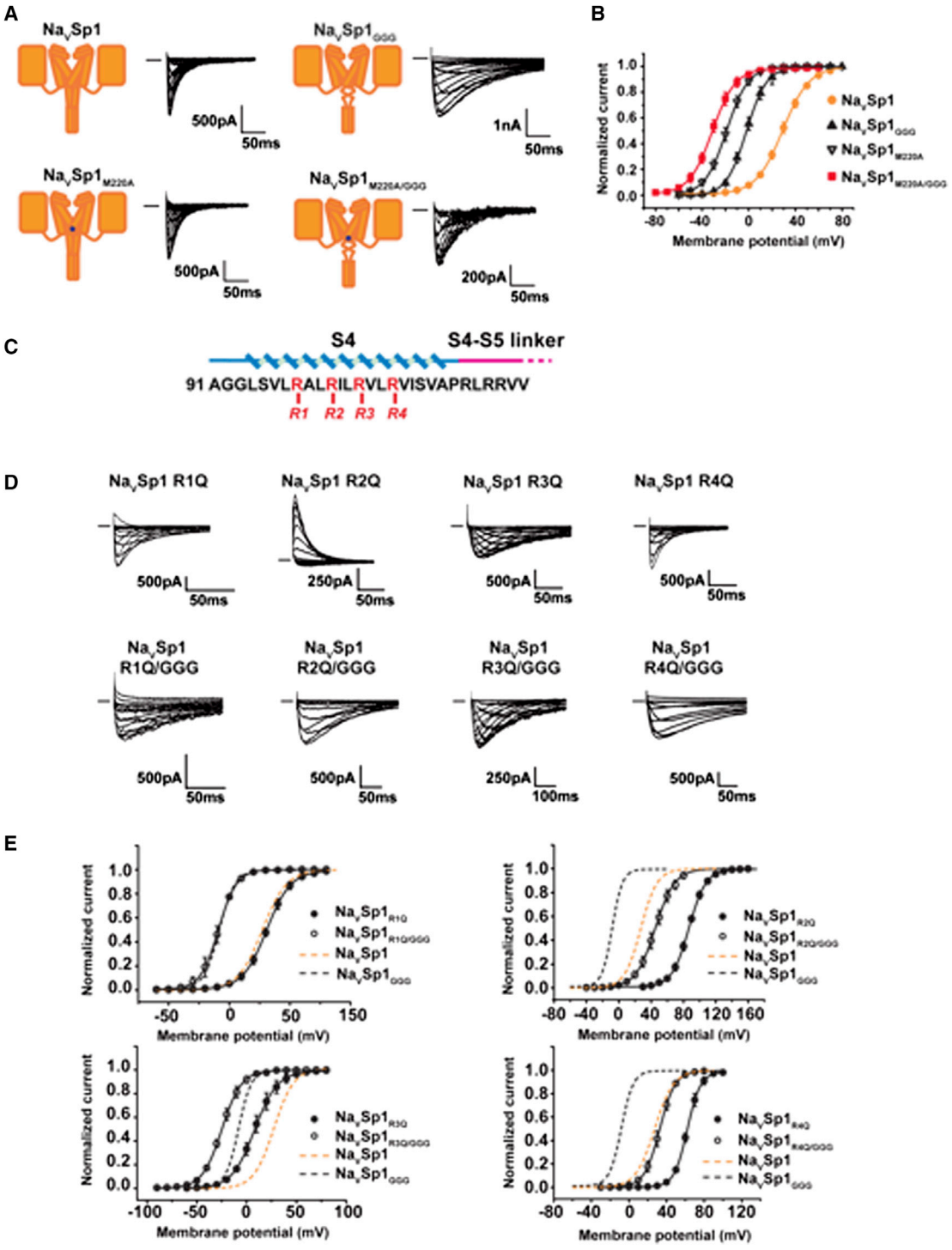

Figure 6. BacNa$_V$ CTD Couples to the Intracellular Gate

(A) Na$_V$Sp1, Na$_V$Sp1$_{GGG}$, Na$_V$Sp1$_{M220A}$, and Na$_V$Sp1$_{M220A/GGG}$ exemplar currents.

(B) Activation curves from (A).

(C) Na$_V$Sp1 S4 mutant sites.

(D) Na$_V$Sp1 R1-R4 and R1-R4/GGG mutant exemplar currents.

(E) Voltage-dependent activation curves for the indicated mutants. Na$_V$Sp1 (tan dashes) and Na$_V$Sp1$_{GGG}$ (black dashes) curves are shown for reference.

See also Table S4.

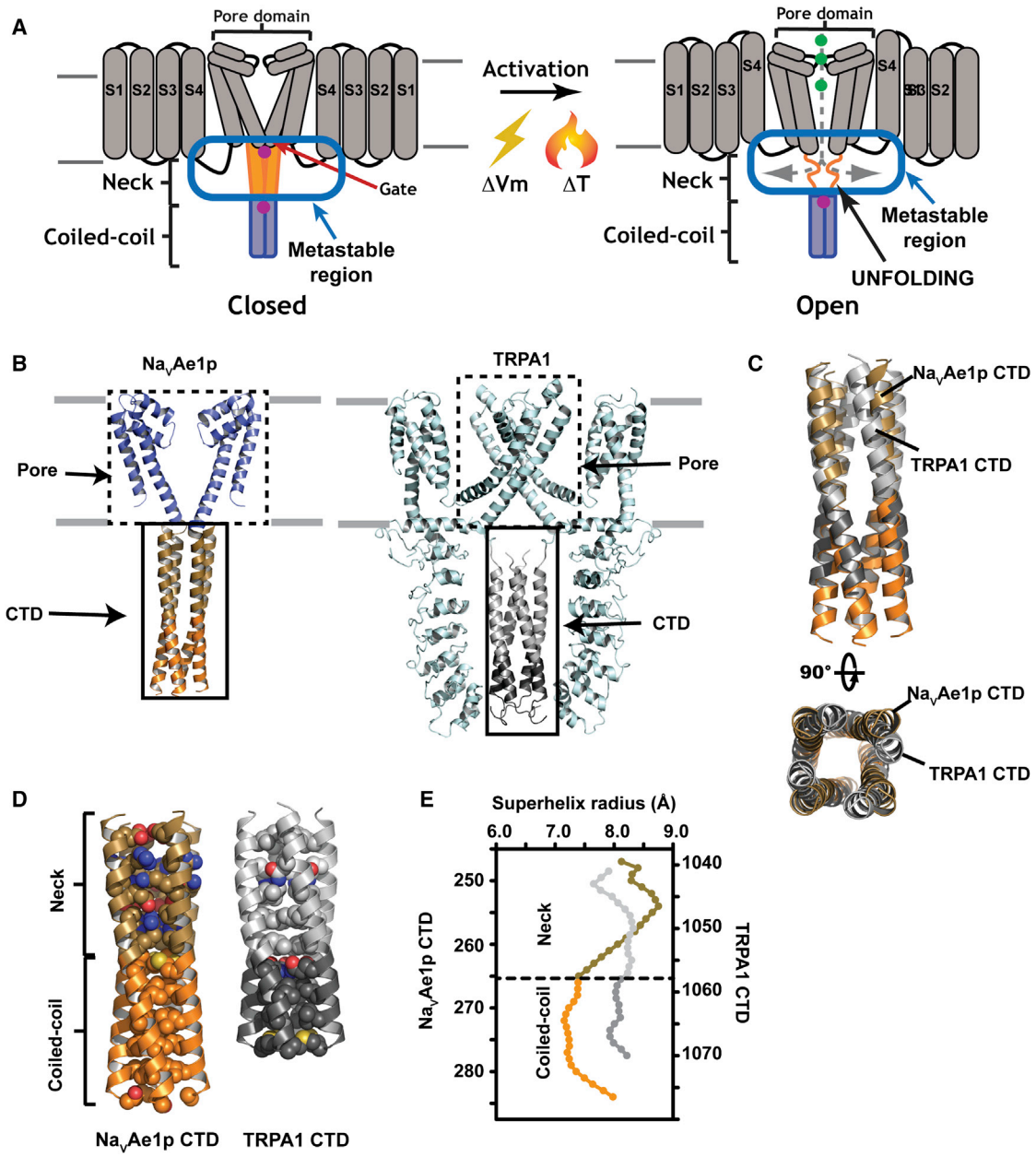

Figure 7. Function and Structural Conservation of VGIC Superfamily CTD Four-Helix Bundles

(A) BacNa$_V$ gating is coupled to a neck unfolding transition. Purple circles indicate neck and coiled-coil ions.

(B) Na$_V$Ae1p (left) and TRPA1 (Paulsen et al., 2015) (right) cartoon diagrams CTD four-helix bundle is indicated.

(C) Na$_V$Ae1p and TRPA1 coiled-coil superposition. TRPA1 shading indicates regions corresponding to the Na$_V$Ae1p neck (light gray) and coiled-coil (dark gray).

(D) Comparison of Na$_V$Ae1p (left) and TRPA1 (right) CTD cores. TRPA1 CTD-buried hydrophilic residues are Gln1047 and Gln1061.

(E) Na$_V$Ae1p and TRPA1 CTD superhelix radii comparison. Colors are as in (C).

See also Table S5.

2012; Shaya et al., 2014). Thus, the clear systemic effects we observe here regarding how neck structure affects activation leads us to propose a gating mechanism in which the order of the neck is directly linked to the ease of channel opening.

Our studies revealed two ion binding sites that contribute to CTD functional properties and neck rigidity. The Na$_V$Ae1 "π-stack" motif is found in other halophile BacNa$_V$s (Figure S7) and may serve as a point of ion-mediated modulation. The coiled-coil ion binding site comprises an E/Q/D/N/A-A-R motif at successive "a"-"d"-"a" positions and is more prevalent among BacNa$_V$s (Figure S7). This structure forms the lower boundary of loss of structure in neck disruptions (Figures 3A,

3B, and S6E) and provides a structural transition between the hydrophobic core of the coiled-coil and more open, hydrophilic core of the neck. The modular nature of the BacNa$_V$ CTD and relatively simple four-helix architecture points toward means to rationally engineer channel responses by controlling the stability of the neck domain using either chimeric approaches or by exploiting stabilizing motifs such as the π-stack.

Some VGIC superfamily members, such as TRPs (Brauchi et al., 2006; Clapham and Miller, 2011; Grandl et al., 2008; Vriens et al., 2014) and K_{2P}s (Bagriantsev et al., 2012; Lolicato et al., 2014; Maingret et al., 2000; Schneider et al., 2014) are gated by temperature. Whether ion channel temperature-dependent responses originate from the action of a single domain (Bagriantsev et al., 2012; Brauchi et al., 2006; Grandl et al., 2008) or a more distributed property (Chowdhury et al., 2014; Clapham and Miller, 2011; Vriens et al., 2014) remains under intense investigation. The Na$_V$Sp1 activation $V_{1/2}$ has a strong temperature dependence (~35 mV over an ~17°C range) that is eliminated by increasing neck disorder (Figures 2D and 2E). Further, Na$_V$Sp1 CTD chimeras having a similar, Na$_V$Sp1$_{PzCTD}$, or more right shifted, Na$_V$Sp1$_{Ab1CTD}$, $V_{1/2}$ responses also show a strong temperature dependence, suggesting that the activation threshold position coincides with a more structured neck. These acute temperature responses contrast with the <5 mV response of the Shaker voltage-gated potassium channel over a similar temperature range (Chowdhury et al., 2014). Although distributed elements may influence BacNa$_V$ temperature responses (DeCaen et al., 2014), particularly in Na$_V$Bh1 (NaChBac), which has a disordered CTD (Powl et al., 2010), our data demonstrate that it is possible for a single domain, the BacNa$_V$ CTD neck, to control the temperature-dependent responses of a VGIC (Figures 2D and 2E). This result provides a definitive example of a defined temperature-sensing domain.

Structural studies of BacNa$_V$s (Shaya et al., 2014), KCNQ channels (Howard et al., 2007; Wiener et al., 2008), and TRP channels (Paulsen et al., 2015; Yu et al., 2012) establish the commonality of parallel four-stranded coiled-coil domains in the VGIC superfamily. Comparison of the Na$_V$Ae1p and TRPA1 CTDs reveals striking similarity well beyond their shared location (Figures 7B and 7C). Superposition shows a close correspondence in the coiled-coil (Figures 7C and 7D; Table S5) and highlights Na$_V$Ae1p neck helix splaying (Figure 7E). The more uniform TRPA1 coiled-coil has two layers of buried hydrophilic residues: an N-terminal one that matches the position of the Na$_V$Ae1p neck and a second one corresponding to the neck:coiled-coil junction (Figures 7C and 7D). Buried hydrophilic residues in coiled-coil cores carry a well-established energetic penalty with respect to quaternary architecture stability (Lupas and Gruber, 2005). Although TRPA1 ankyrin repeats have been implicated in temperature responses (Cordero-Morales et al., 2011; Jabba et al., 2014), it is striking that they form a cage around the CTD (Figure 7B). Hence, many of the reported ankyrin repeat domain effects may be due to modulation of CTD transitions. It is also notable that the voltage-sensor only channel Hv1 has a similar temperature-sensitive membrane proximal coiled-coil domain bearing a buried polar residue in the region implicated in temperature responses (Fujiwara et al., 2012; Takeshita et al., 2014). Thus, the presence of buried polar residues in helical bundle domains in distantly related VGIC superfamily members together with the demonstration that such a metastable domain can play a crucial role in controlling channel function suggests that the mechanism we describe for the BacNa$_V$ CTD may occur in many VGIC superfamily members.

Control of ion channel function by physical and chemical cues is essential for producing dynamic changes in excitability (Hille, 2001). While the coupling between the voltage sensor and pore domains has been studied extensively (Lu et al., 2002; Payandeh et al., 2012; Yifrach and MacKinnon, 2002), mechanisms for how cytoplasmic domains modulate the pore remain imperfectly understood. The four-helix bundle architecture of the BacNa$_V$ CTD provides a simple means to control channel gating. The metastable, but ordered, neck structure directly couples to the energetics of pore opening (Figure 6). This effect does not depend on voltage-sensor movement and likely affects a late step of channel activation. These observations support the idea that conformational changes in such structures can restrain and shape the energetics of channel pore opening (Shaya et al., 2014; Uysal et al., 2009). Consequently, helical bundle domains that bear buried polar residues proximal to a VGIC pore can provide a general mechanism for controlling the action of channels gated by different types of stimuli.

EXPERIMENTAL PROCEDURES

Construct Design and Cloning

Na$_V$Sp1 (*Silicibacter pomeroyi*), Na$_V$Ae1 (*Alkalilimnicola ehrlichii*), chimeras, and mutants were cloned into pIRES2-EGFP vector (Clontech) (Shaya et al., 2014). Chimeric constructs were generated by PCR. Construct boundaries are found in the Supplemental Experimental Procedures. Mutants were made using QuikChange (Stratagene). All constructs were verified by complete DNA sequencing.

Patch-Clamp Electrophysiology

Overexpression and patch-clamp recording from NavSp1, Na$_V$Ae1, mutants, and chimeras were performed as described (Shaya et al., 2014). Voltage dependence was analyzed with the Boltzmann equation, $y = 1/(1 + \exp[(V-V_{1/2})/s])$, where y is fractional activation, V is voltage, $V_{1/2}$ half-activation voltage, and s is the inverse slope factor (mV). Details are found in the Supplemental Experimental Procedures.

Surface Biotinylation Assay

Surface expression was measured in HEK293 cells plated for each HA-tagged construct at 4°C. Samples were analyzed on SDS-PAGE and western blot detected. Details are found in the Supplemental Experimental Procedures.

Protein Purification and Crystallization

Na$_V$Ae1p was expressed and purified as described previously (Shaya et al., 2011, 2014) except that for the size exclusion chromatography step the running buffer included 150 mM NaCl, 50 mM $CaCl_2$, 0.3 mM β-dodecyl maltoside (DDM), 20 mM Na-HEPES, pH (8.0). Constructs for Na$_V$Ae1p-3G and Na$_V$Ae1p-7G were expressed in *Escherichia coli* (DE3) C41 (Miroux and Walker, 1996) using a previously described Na$_V$Ae1p vector (Shaya et al., 2011). Details of expression, purification, and preparation of selenomethionine-labeled Na$_V$Ae1p-3G are found in the Supplemental Experimental Procedures.

Crystallization and Structure Determination

Na$_V$Ae1p crystals were grown by hanging drop vapor diffusion. Na$_V$Ae1p-3G, Na$_V$Ae1p-3G SeMet, and Na$_V$Ae1p-7G crystals were grown by microbatch under oil. Na$_V$Ae1p, Na$_V$Ae1p-NaBr complexes, and Na$_V$Ae1p-3G SeMet diffraction data were collected at Advanced Photon Source Beamline 23ID-B, Argonne National Laboratory. Na$_V$Ae1p-3G and Na$_V$Ae1p-7G diffraction data

were collected at Advanced Light Source Beamline 8.3.1, Lawrence Berkeley National Laboratory. Details for crystallization, data collection, structure determination, and model refinement can be found in the Supplemental Experimental Procedures.

Circular Dichroism Spectroscopy

CD spectra were recorded on an Aviv 215 spectrometer in a 1 mm pathlength quartz cell at 4°C. BacNa$_v$ pore domains were purified as above, exchanged into 10 mM sodium phosphate pH (7.4), 100 mM NaCl, 0.3 mM β-DDM, and concentrated to ~24–26 μM. Wavelength scans were recorded in triplicate from 190 to 320 nm with a 1 nm step size averaged over 10 s. Thermal melts were as described (Shaya et al., 2011).

EPR Labeling and Sample Preparation

Single cysteine mutants of Na$_V$Ae1p, Na$_V$Ae1p-3G, and Na$_V$Sp1p were generated by quick-change mutagenesis and were purified as above using 1 mM TCEP in all buffers and labeled with MTSSL. CW-spectra were collected on a Bruker EMX at 10 mW power with a modulation amplitude of 1.6G. All spectra were normalized to the double integral. DEER experiments were carried out using a standard four-pulse protocol (Jeschke, 2002). Details can be found in the Supplemental Experimental Procedures.

ACCESSION NUMBERS

The accession numbers for the Coordinates and structure factors reported in this paper are RCSB PDB: 5HJ8, 5HK6, 5HKD, 5HK7, 5HKT, and 5HKU.

SUPPLEMENTAL INFORMATION

Supplemental Information includes Supplemental Experimental Procedures, seven figures, and five tables and can be found with this article online at http://dx.doi.org/10.1016/j.cell.2016.02.001.

AUTHOR CONTRIBUTIONS

C.A., A.R., and D.L.M. conceived the study and designed the experiments. C.A., A.R., D.S., F.F., R.A.S., S.R.N., and S.M. performed the experiments. C.A. performed electrophysiological experiments and analyzed the data. A.R., D.S., and S.R.N. purified the proteins. A.R. crystallized and determined the structures of polyglycine mutants, performed the CD experiments, prepared EPR samples, and analyzed the data. D.S. grew the Na$_V$Ae1p crystals, collected the data, and solved the structure. F.F. solved and refined the structures and analyzed the data. A.R., S.M., and S.A.R. prepared the EPR samples. S.M. and S.A.R. collected the EPR data. H.S.M. supervised the EPR experiments. A.R., R.A.S., H.S.M., and D.L.M. analyzed the EPR data. D.L.M. analyzed the data and provided guidance and support throughout. C.A., A.R., D.S., F.F., R.A.S., H.S.M., and D.L.M. wrote the paper.

ACKNOWLEDGMENTS

We thank M. Grabe, L. Jan, A. Moroni, and the D.L.M. lab members for manuscript comments. This work was supported by grants U54 GM087519 to H.S.M., R01-HL080050, R01-DC007664, and U54-GM094625 to D.L.M., and to C.A. from the American Heart Association. C.A. is an AHA postdoctoral fellow.

Received: August 7, 2015
Revised: December 22, 2015
Accepted: January 28, 2016
Published: February 25, 2016

REFERENCES

Bagnéris, C., Decaen, P.G., Hall, B.A., Naylor, C.E., Clapham, D.E., Kay, C.W., and Wallace, B.A. (2013). Role of the C-terminal domain in the structure and function of tetrameric sodium channels. Nat. Commun. *4*, 2465.

Bagriantsev, S.N., Clark, K.A., and Minor, D.L., Jr. (2012). Metabolic and thermal stimuli control K(2P)2.1 (TREK-1) through modular sensory and gating domains. EMBO J. *31*, 3297–3308.

Berova, N., Nakanishi, K., and Woody, R.W. (2000). Circular Dichroism: Principles and Applications, Second Edition (Wiley-VCH).

Brauchi, S., Orta, G., Salazar, M., Rosenmann, E., and Latorre, R. (2006). A hot-sensing cold receptor: C-terminal domain determines thermosensation in transient receptor potential channels. J. Neurosci. *26*, 4835–4840.

Chowdhury, S., Jarecki, B.W., and Chanda, B. (2014). A molecular framework for temperature-dependent gating of ion channels. Cell *158*, 1148–1158.

Clapham, D.E., and Miller, C. (2011). A thermodynamic framework for understanding temperature sensing by transient receptor potential (TRP) channels. Proc. Natl. Acad. Sci. USA *108*, 19492–19497.

Cordero-Morales, J.F., Gracheva, E.O., and Julius, D. (2011). Cytoplasmic ankyrin repeats of transient receptor potential A1 (TRPA1) dictate sensitivity to thermal and chemical stimuli. Proc. Natl. Acad. Sci. USA *108*, E1184–E1191.

DeCaen, P.G., Yarov-Yarovoy, V., Sharp, E.M., Scheuer, T., and Catterall, W.A. (2009). Sequential formation of ion pairs during activation of a sodium channel voltage sensor. Proc. Natl. Acad. Sci. USA *106*, 22498–22503.

DeCaen, P.G., Takahashi, Y., Krulwich, T.A., Ito, M., and Clapham, D.E. (2014). Ionic selectivity and thermal adaptations within the voltage-gated sodium channel family of alkaliphilic Bacillus. eLife *3*.

Fujiwara, Y., Kurokawa, T., Takeshita, K., Kobayashi, M., Okochi, Y., Nakagawa, A., and Okamura, Y. (2012). The cytoplasmic coiled-coil mediates cooperative gating temperature sensitivity in the voltage-gated H(+) channel Hv1. Nat. Commun. *3*, 816.

Grandl, J., Hu, H., Bandell, M., Bursulaya, B., Schmidt, M., Petrus, M., and Patapoutian, A. (2008). Pore region of TRPV3 ion channel is specifically required for heat activation. Nat. Neurosci. *11*, 1007–1013.

Hille, B. (2001). Ion Channels of Excitable Membranes, Third Edition (Sinauer Associates, Inc.).

Howard, R.J., Clark, K.A., Holton, J.M., and Minor, D.L., Jr. (2007). Structural insight into KCNQ (Kv7) channel assembly and channelopathy. Neuron *53*, 663–675.

Irie, K., Kitagawa, K., Nagura, H., Imai, T., Shimomura, T., and Fujiyoshi, Y. (2010). Comparative study of the gating motif and C-type inactivation in prokaryotic voltage-gated sodium channels. J. Biol. Chem. *285*, 3685–3694.

Irie, K., Shimomura, T., and Fujiyoshi, Y. (2012). The C-terminal helical bundle of the tetrameric prokaryotic sodium channel accelerates the inactivation rate. Nat. Commun. *3*, 793.

Jabba, S., Goyal, R., Sosa-Pagán, J.O., Moldenhauer, H., Wu, J., Kalmeta, B., Bandell, M., Latorre, R., Patapoutian, A., and Grandl, J. (2014). Directionality of temperature activation in mouse TRPA1 ion channel can be inverted by single-point mutations in ankyrin repeat six. Neuron *82*, 1017–1031.

Jeschke, G. (2002). Distance measurements in the nanometer range by pulse EPR. Chemphyschem *3*, 927–932.

Jiang, Y., Lee, A., Chen, J., Cadene, M., Chait, B.T., and MacKinnon, R. (2002). Crystal structure and mechanism of a calcium-gated potassium channel. Nature *417*, 515–522.

Koishi, R., Xu, H., Ren, D., Navarro, B., Spiller, B.W., Shi, Q., and Clapham, D.E. (2004). A superfamily of voltage-gated sodium channels in bacteria. J. Biol. Chem. *279*, 9532–9538.

Lolicato, M., Riegelhaupt, P.M., Arrigoni, C., Clark, K.A., and Minor, D.L., Jr. (2014). Transmembrane helix straightening and buckling underlies activation of mechanosensitive and thermosensitive K(2P) channels. Neuron *84*, 1198–1212.

Lu, Z., Klem, A.M., and Ramu, Y. (2002). Coupling between voltage sensors and activation gate in voltage-gated K+ channels. J. Gen. Physiol. *120*, 663–676.

Lupas, A.N., and Gruber, M. (2005). The structure of α-helical coiled coils. Adv. Protein Chem. *70*, 37–78.

Maingret, F., Lauritzen, I., Patel, A.J., Heurteaux, C., Reyes, R., Lesage, F., Lazdunski, M., and Honoré, E. (2000). TREK-1 is a heat-activated background K(+) channel. EMBO J. *19*, 2483–2491.

McCusker, E.C., Bagnéris, C., Naylor, C.E., Cole, A.R., D'Avanzo, N., Nichols, C.G., and Wallace, B.A. (2012). Structure of a bacterial voltage-gated sodium channel pore reveals mechanisms of opening and closing. Nat. Commun. *3*, 1102.

Mchaourab, H.S., Steed, P.R., and Kazmier, K. (2011). Toward the fourth dimension of membrane protein structure: insight into dynamics from spin-labeling EPR spectroscopy. Structure *19*, 1549–1561.

Mio, K., Mio, M., Arisaka, F., Sato, M., and Sato, C. (2010). The C-terminal coiled-coil of the bacterial voltage-gated sodium channel NaChBac is not essential for tetramer formation, but stabilizes subunit-to-subunit interactions. Prog. Biophys. Mol. Biol. *103*, 111–121.

Miroux, B., and Walker, J.E. (1996). Over-production of proteins in Escherichia coli: mutant hosts that allow synthesis of some membrane proteins and globular proteins at high levels. J. Mol. Biol. *260*, 289–298.

Morais-Cabral, J.H., and Robertson, G.A. (2015). The enigmatic cytoplasmic regions of KCNH channels. J. Mol. Biol. *427*, 67–76.

Paulsen, C.E., Armache, J.P., Gao, Y., Cheng, Y., and Julius, D. (2015). Structure of the TRPA1 ion channel suggests regulatory mechanisms. Nature *520*, 511–517.

Pavlov, E., Bladen, C., Winkfein, R., Diao, C., Dhaliwal, P., and French, R.J. (2005). The pore, not cytoplasmic domains, underlies inactivation in a prokaryotic sodium channel. Biophys. J. *89*, 232–242.

Payandeh, J., and Minor, D.L., Jr. (2015). Bacterial voltage-gated sodium channels (BacNa(V)s) from the soil, sea, and salt lakes enlighten molecular mechanisms of electrical signaling and pharmacology in the brain and heart. J. Mol. Biol. *427*, 3–30.

Payandeh, J., Scheuer, T., Zheng, N., and Catterall, W.A. (2011). The crystal structure of a voltage-gated sodium channel. Nature *475*, 353–358.

Payandeh, J., Gamal El-Din, T.M., Scheuer, T., Zheng, N., and Catterall, W.A. (2012). Crystal structure of a voltage-gated sodium channel in two potentially inactivated states. Nature *486*, 135–139.

Pioletti, M., Findeisen, F., Hura, G.L., and Minor, D.L., Jr. (2006). Three-dimensional structure of the KChIP1-Kv4.3 T1 complex reveals a cross-shaped octamer. Nat. Struct. Mol. Biol. *13*, 987–995.

Powl, A.M., O'Reilly, A.O., Miles, A.J., and Wallace, B.A. (2010). Synchrotron radiation circular dichroism spectroscopy-defined structure of the C-terminal domain of NaChBac and its role in channel assembly. Proc. Natl. Acad. Sci. USA *107*, 14064–14069.

Ren, D., Navarro, B., Xu, H., Yue, L., Shi, Q., and Clapham, D.E. (2001). A prokaryotic voltage-gated sodium channel. Science *294*, 2372–2375.

Scheuer, T. (2014). Bacterial sodium channels: models for eukaryotic sodium and calcium channels. Handbook Exp. Pharmacol. *221*, 269–291.

Schneider, E.R., Anderson, E.O., Gracheva, E.O., and Bagriantsev, S.N. (2014). Temperature sensitivity of two-pore (K2P) potassium channels. Curr. Top. Membr. *74*, 113–133.

Shaya, D., Kreir, M., Robbins, R.A., Wong, S., Hammon, J., Brüggemann, A., and Minor, D.L., Jr. (2011). Voltage-gated sodium channel (NaV) protein dissection creates a set of functional pore-only proteins. Proc. Natl. Acad. Sci. USA *108*, 12313–12318.

Shaya, D., Findeisen, F., Abderemane-Ali, F., Arrigoni, C., Wong, S., Nurva, S.R., Loussouarn, G., and Minor, D.L., Jr. (2014). Structure of a prokaryotic sodium channel pore reveals essential gating elements and an outer ion binding site common to eukaryotic channels. J. Mol. Biol. *426*, 467–483.

Takeshita, K., Sakata, S., Yamashita, E., Fujiwara, Y., Kawanabe, A., Kurokawa, T., Okochi, Y., Matsuda, M., Narita, H., Okamura, Y., and Nakagawa, A. (2014). X-ray crystal structure of voltage-gated proton channel. Nat. Struct. Mol. Biol. *21*, 352–357.

Tang, L., Gamal El-Din, T.M., Payandeh, J., Martinez, G.Q., Heard, T.M., Scheuer, T., Zheng, N., and Catterall, W.A. (2014). Structural basis for Ca2+ selectivity of a voltage-gated calcium channel. Nature *505*, 56–61.

Tsai, C.J., Tani, K., Irie, K., Hiroaki, Y., Shimomura, T., McMillan, D.G., Cook, G.M., Schertler, G.F., Fujiyoshi, Y., and Li, X.D. (2013). Two alternative conformations of a voltage-gated sodium channel. J. Mol. Biol. *425*, 4074–4088.

Ulmschneider, M.B., Bagnéris, C., McCusker, E.C., Decaen, P.G., Delling, M., Clapham, D.E., Ulmschneider, J.P., and Wallace, B.A. (2013). Molecular dynamics of ion transport through the open conformation of a bacterial voltage-gated sodium channel. Proc. Natl. Acad. Sci. USA *110*, 6364–6369.

Uysal, S., Vásquez, V., Tereshko, V., Esaki, K., Fellouse, F.A., Sidhu, S.S., Koide, S., Perozo, E., and Kossiakoff, A. (2009). Crystal structure of full-length KcsA in its closed conformation. Proc. Natl. Acad. Sci. USA *106*, 6644–6649.

Vargas, E., Yarov-Yarovoy, V., Khalili-Araghi, F., Catterall, W.A., Klein, M.L., Tarek, M., Lindahl, E., Schulten, K., Perozo, E., Bezanilla, F., and Roux, B. (2012). An emerging consensus on voltage-dependent gating from computational modeling and molecular dynamics simulations. J. Gen. Physiol. *140*, 587–594.

Vriens, J., Nilius, B., and Voets, T. (2014). Peripheral thermosensation in mammals. Nat. Rev. Neurosci. *15*, 573–589.

Wiener, R., Haitin, Y., Shamgar, L., Fernández-Alonso, M.C., Martos, A., Chomsky-Hecht, O., Rivas, G., Attali, B., and Hirsch, J.A. (2008). The KCNQ1 (Kv7.1) COOH terminus, a multitiered scaffold for subunit assembly and protein interaction. J. Biol. Chem. *283*, 5815–5830.

Yang, H., Zhang, G., and Cui, J. (2015). BK channels: multiple sensors, one activation gate. Front. Physiol. *6*, 29.

Yifrach, O., and MacKinnon, R. (2002). Energetics of pore opening in a voltage-gated K(+) channel. Cell *111*, 231–239.

Yu, F.H., Yarov-Yarovoy, V., Gutman, G.A., and Catterall, W.A. (2005). Overview of molecular relationships in the voltage-gated ion channel superfamily. Pharmacol. Rev. *57*, 387–395.

Yu, Y., Ulbrich, M.H., Li, M.H., Dobbins, S., Zhang, W.K., Tong, L., Isacoff, E.Y., and Yang, J. (2012). Molecular mechanism of the assembly of an acid-sensing receptor ion channel complex. Nat. Commun. *3*, 1252.

Yuan, P., Leonetti, M.D., Pico, A.R., Hsiung, Y., and MacKinnon, R. (2010). Structure of the human BK channel Ca2+-activation apparatus at 3.0 A resolution. Science *329*, 182–186.

Zagotta, W.N., Olivier, N.B., Black, K.D., Young, E.C., Olson, R., and Gouaux, E. (2003). Structural basis for modulation and agonist specificity of HCN pacemaker channels. Nature *425*, 200–205.

Zhang, X., Ren, W., DeCaen, P., Yan, C., Tao, X., Tang, L., Wang, J., Hasegawa, K., Kumasaka, T., He, J., et al. (2012). Crystal structure of an orthologue of the NaChBac voltage-gated sodium channel. Nature *486*, 130–134.